JACS
JOURNAL OF THE AMERICAN CHEMICAL SOCIETY
pubs.acs.org/JACS
Article

Layered Semiconductor $Cr_{0.32}Ga_{0.68}Te_{2.33}$ with Concurrent Broken Inversion Symmetry and Ferromagnetism: A Bulk Ferrovalley Material Candidate

Yingdong Guan,[+] Leixin Miao,[+] Jingyang He, Jinliang Ning, Yangyang Chen, Weiwei Xie, Jianwei Sun, Venkatraman Gopalan, Jun Zhu, Xiaoping Wang, Nasim Alem,* Qiang Zhang,* and Zhiqiang Mao*

Cite This: *J. Am. Chem. Soc.* 2023, 145, 4683−4690

ABSTRACT: The valleytronic state found in group-VI transition-metal dichalcogenides such as MoS_2 has attracted immense interest since its valley degree of freedom could be used as an information carrier. However, valleytronic applications require spontaneous valley polarization. Such an electronic state is predicted to be accessible in a new ferroic family of materials, i.e., ferrovalley materials, which features the coexistence of spontaneous spin and valley polarization. Although many atomic monolayer materials with hexagonal lattices have been predicted to be ferrovalley materials, no bulk ferrovalley material candidates have been reported or proposed. Here, we show that a new non-centrosymmetric van der Waals (vdW) semiconductor $Cr_{0.32}Ga_{0.68}Te_{2.33}$, with intrinsic ferromagnetism, is a possible candidate for bulk ferrovalley material. This material exhibits several remarkable characteristics: (i) it forms a natural heterostructure between vdW gaps, a quasi-two-dimensional (2D) semiconducting Te layer with a honeycomb lattice stacked on the 2D ferromagnetic slab comprised of the (Cr, Ga)-Te layers, and (ii) the 2D Te honeycomb lattice yields a valley-like electronic structure near the Fermi level, which, in combination with inversion symmetry breaking, ferromagnetism, and strong spin-orbit coupling contributed by heavy Te element, creates a possible bulk spin-valley locked electronic state with valley polarization as suggested by our DFT calculations. Further, this material can also be easily exfoliated to 2D atomically thin layers. Therefore, this material offers a unique platform to explore the physics of valleytronic states with spontaneous spin and valley polarization in both bulk and 2D atomic crystals.

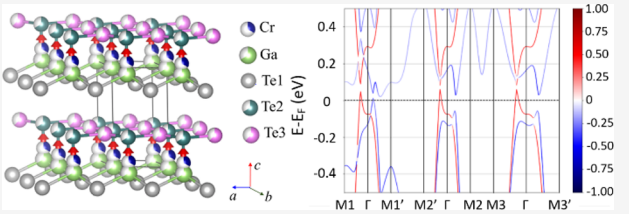

1. INTRODUCTION

Among two-dimensional (2D) materials, one family of material, i.e., monolayers of group-VI transition metal dichalcogenides (TMDCs) such as MoS_2, is of particular interest.[1−7] These materials not only possess an active valley degree of freedom but are also characterized by inversion symmetry breaking and strong spin-orbit coupling (SOC). The combination of these traits creates a unique electronic state featuring spin-valley locking.[1−7] Such spin-valley-locked states generate distinct topological valley transport properties such as the valley Hall effect, spin Hall effect, and photo-induced charge Hall effect.[7−9] These exotic properties have great potential for applications in valleytronics and spintronics.[10] However, the realization of these applications requires control of valley polarization. Significant efforts have been devoted to finding ways of lifting valley degeneracy, which have led to significant experimental progress. External stimuli such as optical pumping,[3,4,11] external magnetic fields,[12] and magnetic doping[13−15] have shown effectiveness in creating valley polarization. However, these means are difficult to be implemented in valleytronic devices for practical applications. Optical pumping is a dynamic process that cannot be used for device operations for information storage. Magnetic field-driven valley polarization requires extremely strong magnetic fields, which are not accessible in real devices. Magnetic doping can induce strong disordering scattering, which is also unfavorable for device operations.

Another recently established approach is to use the interfacial magnetic proximity effect in heterostructures to achieve valley polarization control.[16−21] For instance, the heterostructure formed by a 2D ferromagnetic (FM) semiconductor CrI_3 and a WSe_2 monolayer enabled unprecedented control of spin and valley pseudospin in WSe_2 and rapid switching of valley splitting and polarization using magnetization flipping.[21] In addition to the heterostructure strategy, there have been significant theoretical efforts aiming at predicting 2D valleytronic materials with intrinsic ferromagnetism, which are named ferrovalley materials.[22] If such

Received: December 2, 2022
Published: February 16, 2023

https://doi.org/10.1021/jacs.2c12848
J. Am. Chem. Soc. 2023, 145, 4683−4690

materials could be realized, it would avoid challenges in fabricating complex heterostructures and enable valley polarization switching via magnetization flipping. We note that a number of monolayer ferrovalley materials have been predicted in the literature, including 2H-VSe_2,[22] 2H-$LaBr_2$,[23] 2H-GdX_2 (X = I, F, Cl, and Br),[24,25] $VAgP_2Se_6$,[26] Nb_3I_8,[27] $TiVI_6$,[28] VSi_2N_4,[29] Cr_2CoF,[30] NbX_2 (X = S, Se),[31] Janus 2H-VSSe,[32] and 2H-LaBrI.[33] Although these predictions are yet to be verified experimentally, it points to a promising direction for the practical control of spin and valley polarization in valleytronic devices.

In this study, we report a new non-centrosymmetric van der Waals (vdW) semiconductor $Cr_{0.32}Ga_{0.68}Te_{2.33}$ with intrinsic ferromagnetism, which is a possible candidate for bulk ferrovalley material. This material forms a natural heterostructure composed of a 2D FM layer and a 2D semiconducting layer between vdW gaps. Its ferromagnetism originates from the 2D Cr sublattice, while the 2D Te honeycomb lattice forms its 2D semiconducting layer. One distinct characteristic of such a heterostructure is the natural combination of inversion symmetry breaking, strong SOC induced by heavy Te element, ferromagnetism, and active valley degree of freedom enabled by the honeycomb Te lattice. Our DFT band structure calculations suggest that such a natural heterostructure generates a valleytronic state with spontaneous valley polarization. Moreover, we find that this material can be mechanically exfoliated to 2D atomically thin layers. Given that the single crystals of $Cr_{0.32}Ga_{0.68}Te_{2.33}$ can be easily synthesized and its magnetization is large ($\sim 3.0\mu_B$/Cr) and can be controlled by the magnetic field, it offers a promising platform for exploring the tunability of spin and valley polarization via magnetization manipulation and seeking anomalous valley Hall effect[22] in bulk and 2D atomic crystals.

2. RESULTS AND DISCUSSION

Single crystals of $Cr_{0.32}Ga_{0.68}Te_{2.33}$ (Figure 1d) were synthesized using a flux method (see the Methods). We performed single-crystal X-ray diffraction (XRD) as well as neutron diffraction measurements to determine the crystal structure of this material. The structure refinement based on these measurements (see the Methods) shows that this material crystallizes in a non-centrosymmetric trigonal

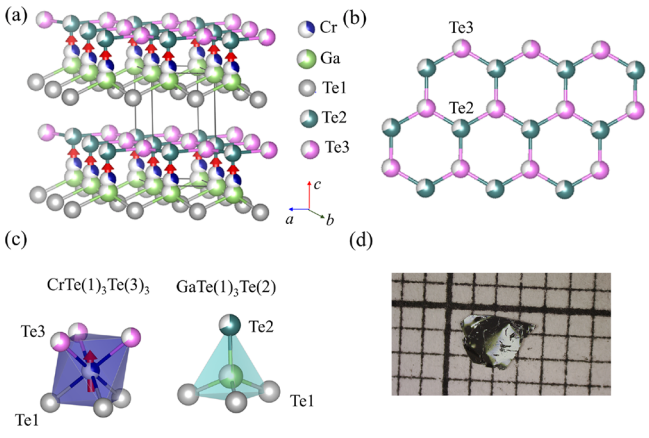

Figure 1. (a) Crystal and magnetic structure of $Cr_{0.32}Ga_{0.68}Te_{2.33}$. (b) Honeycomb lattice formed by Te(2) and Te(3) atoms. (c) Octahedral environment of Cr and tetrahedral environment of Ga. (d) Picture of a typical $Cr_{0.32}Ga_{0.68}Te_{2.33}$ crystal.

structure with the space group of $P3$ (no. 143). The composition resulting from the refinement is $Cr_{0.32}Ga_{0.68}Te_{2.33}$, consistent with the averaged composition measured by X-ray energy-dispersive spectroscopy (EDS), $Cr_{0.32}Ga_{0.69}Te_{2.20}$ (note that the measured ratio of Cr/Ga to Te has a relatively larger uncertainty due to the large discrepancy in the atomic mass between Te and Cr/Ga). Figure 1a presents the schematic of the structure of $Cr_{0.32}Ga_{0.68}Te_{2.33}$, which exhibits several interesting characteristics. First, this structure is layered with a vdW gap and built of the stacking of Te(1)-[Ga, Cr]-[Te(2), Te(3)] atomic layers along the c axis. Te(1), Te(2), and Te(3) represent the Te atoms that occupy three distinct sites in the unit cell. Te(2) and Te(3), while showing a tiny discrepancy in the c axis coordinate (see Table 1), form a quasi-2D honeycomb lattice, as shown in Figure 1b. Nevertheless, such a quasi-2D honeycomb lattice is imperfect, and there are abundant vacancies on both Te(2) and Te(3) sites. The occupancies of Te(2) and Te(3) are 68.3 and 64.4%, respectively. Second, the Cr and Ga sites are not fully occupied either, with occupancies of 31.7% for Cr and 68.3% for Ga; Cr is slightly shifted (~0.77 Å) along the c axis relative to Ga (see Figure 1a). Third, Ga and Cr display different coordination with Te; Ga is tetrahedrally coordinated with Te(2) and Te(1), whereas Cr is octahedrally coordinated with Te(1) and Te(3) (see Figure 1c). Since Ga is bounded with Te(2) but not with Te(3), the occupancy of the Ga site is the same as that of the Te(2) site (i.e., 68.3%). There is no structural transition from 300 K down to 4 K. The structural parameters determined from the fits to the neutron diffraction results at 4 K are summarized in Table 1.

We further performed scanning transmission electron microscopy (STEM) analyses on $Cr_{0.32}Ga_{0.68}Te_{2.33}$ to confirm its structure determined by the neutron diffraction experiment. Figure 2a,b shows the high-angle annular dark-field (HAADF) STEM images from the [100] and [001] zone axes. The insets in Figure 2 show the magnified images from the regions highlighted by the dashed red and blue boxes, respectively. The crystal structure models refined from the neutron diffraction are superimposed onto the STEM images in the insets. The HAADF-STEM image from the [100] zone axis in Figure 2a reveals the atomic arrangement of the layered crystal structure formed by the stacking of the Te(1)-(Ga, Cr)-[Te(2), Te(3)] slabs, which shows a good agreement with the structure model refined from neutron diffraction spectra. The intensity of the atomic columns of Te(2) and Te(3) show variations (see Supplementary Figure S1), indicating the presence of vacancies on both sites; this agrees with the site occupancy of 68.3% for Te(2) and 64.4% for Te(3) derived from the neutron diffraction structure refinement. In contrast, the intensity of the atomic columns of Te(1) remains constant (Figure S1), consistent with the occupancy of 1.0 fitted by the neutron diffraction. For the atomic columns occupied by the Ga and Cr ions (1a site), it also exhibits intensity variation. Moreover, their atomic columns are slightly elongated along the c axis, which corroborates the abovementioned slight atomic position shift ($\sim$ 0.77 Å) of Cr relative to Ga along the c axis. The HAADF-STEM image from the [001] zone axis in Figure 2b shows the projection of the staggered stacking of the [Te(2), Te(3)] honeycomb lattice on the (Cr/Ga)Te(1) lattice. Numerous vacancies on the Te(3) sites are discernable, as manifested by their relatively lower intensity. As an example, the red dashed circle in the inset of Figure 2b highlights a vacancy site of Te(3). Additionally, we also observed

https://doi.org/10.1021/jacs.2c12848
J. Am. Chem. Soc. 2023, 145, 4683−4690

Table 1. Atomic Coordinates, Occupancy, and Anisotropic Thermal Parameters for $Cr_{0.32}Ga_{0.68}Te_{2.33}$ Determined from the Fits to the Squared Structural Factors of the Nuclear Peaks Collected at Neutron Single-Crystal Diffractometer TOPAZ at 4 K[a]

atom	Wyckoff	occupancy	x	y	z	$U_{11} = U_{22}$	U_{33}	U_{12}
Cr	1*a*	0.317(5)	0	0	0.1116(5)	0.0040(2)	0.0104(2)	0.00202(11)
Ga	1*a*	0.683(6)	0	0	0	0.0040(2)	0.0104(2)	0.00202(11)
Te1	1*c*	1	2/3	1/3	0.8594(2)	0.0160(5)	0.0678(11)	0.0080(2)
Te2	1*a*	0.683(9)	0	0	0.3615(2)	0.0858(3)	0.0115 (5)	0.0429(6)
Te3	1*b*	0.644(7)	1/3	2/3	0.3723(3)	0.141(3)	0.0161 (9)	0.0705(14)

[a]The space group *P*3 (no. 143) has been identified with lattice parameters, $a = b = 4.0219(2)$ Å, $c = 7.0560(3)$ Å, $\alpha = \beta = 90°$, and $\gamma = 120°$.

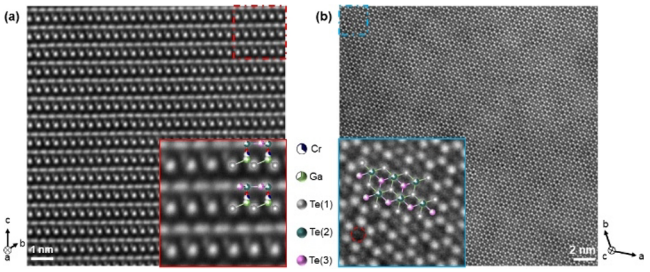

Figure 2. HAADF-STEM images of the $Cr_{0.32}Ga_{0.68}Te_{2.33}$ acquired from (a) [100] and (b) [001] zone axes. The insets are the magnified images from the region highlighted by the dashed red and blue boxes, respectively, with the crystal model from neutron diffraction superimposed. The dashed red circle in (b) highlights one of the vacancies on the Te(3) site.

incommensurate diffuse scattering in the selected area electron diffraction (SAED) patterns taken along the [100] and [001] zone axes (Supplementary Figure S2), suggesting the emergence of short-range ordering in the structure. Since Cr and Ga form octahedral and tetrahedral coordination with Te, respectively, short-range ordering of the $CrTe(1)_3Te(3)_3$ octahedra and $GaTe(1)_3Te(2)$ tetrahedra may lead to short-range ordering of Te(2) and Te(3), which might be the origin of the observed diffusive incommensurate diffraction spots in Figure S2.

Another important structural characteristic of $Cr_{0.32}Ga_{0.68}Te_{2.33}$ is its inversion symmetry breaking, as manifested by its non-centrosymmetric space group *P*3. We have verified this feature through second harmonic generation (SHG) measurements. SHG, defined as $P_i^{2\omega} \propto d_{ijk}E_j^{\omega}E_k^{\omega}$, is the second-order nonlinear optical process that occurs only in materials lacking inversion centers. Because of its sensitivity to the crystal structure, it can be applied to characterize the point group of the material. The SHG polarimetry was employed to extract the point group of $Cr_{0.32}Ga_{0.68}Te_{2.33}$. The linearly polarized incident electric field was rotated by an angle of ψ and focused on the crystal whose $[2\bar{1}\bar{1}0]$ and $[01\bar{1}0]$ axes were parallel to the lab *X* and *Y* axes, respectively, as shown in Figure 3a. The generated SHG intensities were collected by the photo-multiplier tube detector after decomposing into *p*-polarized (∥) and *s*-polarized (⊥) light. As shown in Figure 3b, six sets of polarimetry data measured with three different incident angles α were fitted simultaneously to three different models based on the point groups of 3, 32, and 3*m*. We found that the model of point group 3 yields the best fit, which is consistent with the *P*3 structure determined by the neutron diffraction experiment.

In addition to structure determination, we have also characterized the electronic and magnetic properties of $Cr_{0.32}Ga_{0.68}Te_{2.33}$ and found that it is an FM semiconductor

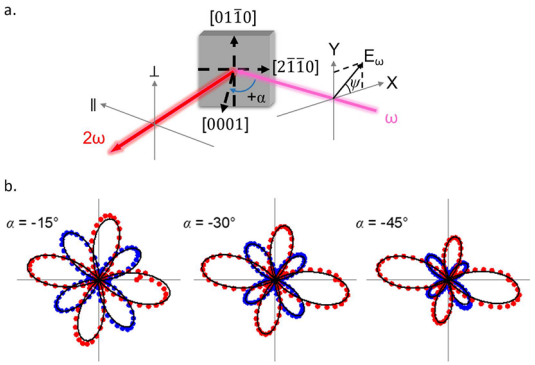

Figure 3. (a) Schematics of the SHG experiment. (b) Polar plots of $Cr_{0.32}Ga_{0.68}Te_{2.33}$ measured at three incident angles. The blue and red dots correspond to the *p*-polarized (∥) and *s*-polarized (⊥) SHG response, respectively. The black line is the theoretical fit for point group 3.

with a narrow direct band gap. Its ferromagnetism is revealed from magnetization measurements. Figure 4a,c shows its temperature dependences of magnetic susceptibility χ measured with a magnetic field of 1000 Oe applied to the in-plane (H∥ab) and out-of-plane (H⊥ab) directions, respectively, under zero-field cooling (ZFC) and field cooling (FC) histories. A sharp magnetic transition near 20 K was observed in these measurements. To reveal the nature of this magnetic

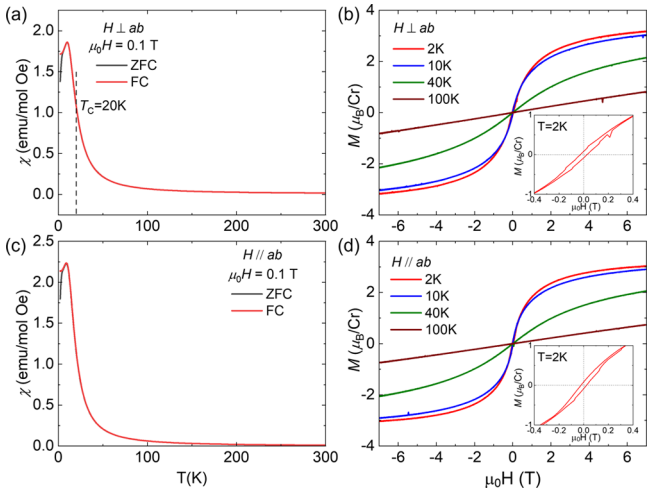

Figure 4. (a, c) Temperature dependence of magnetic susceptibility measured under ZFC and FC histories for $Cr_{0.32}Ga_{0.68}Te_{2.33}$ with (a) H⊥ab configuration and (c) H∥ab configuration. Isothermal magnetization with (b) the H⊥ab-plane and (d) the H∥ab-plane at various temperatures. Inset: enlarged isothermal magnetization with (b) the H⊥ab-plane and (d) the H∥ab-plane at $T = 2$ K.

https://doi.org/10.1021/jacs.2c12848
J. Am. Chem. Soc. 2023, 145, 4683−4690

transition, we have also measured its isothermal magnetization at various temperatures under H||ab and H⊥ab configurations, respectively. The data from these measurements, presented in Figure 4b,d, show clear FM polarization upon magnetic field sweeps, indicating that the magnetic transition near 20 K should correspond to an FM transition. Moreover, we observed small magnetic hysteresis in the field sweeps of magnetization below T_c (~20 K), with the a coercive field of 300 Oe (see the inset in Figure 4b,d), indicating that $Cr_{0.32}Ga_{0.68}Te_{2.33}$ should be a soft ferromagnet. In its polarized FM state at 7 T, we find that its saturated magnetic moment M_s is ~3.02 μ_B/Cr for H||ab and 3.16 μ_B/Cr for H||c, consistent with the ground spin state of S = 3/2 for Cr^{3+}. The slightly greater M_s for H||c than for H||ab implies that its spin easy axis is along the *c* axis. Our symmetry analysis based on the refined crystal structure from neutron diffraction indicates that the out-of-plane FM order with the magnetic space group *P*3 (no. 143.1) (Figure 1a) is indeed the only symmetry-allowed FM structure with a maximal magnetic space group in $Cr_{0.32}Ga_{0.68}Te_{2.33}$.[34] Nevertheless, our temperature-dependent neutron scattering measurements did not find a clear increase in neutron scattering intensity in low-Q peaks such as (010), (−110), (−111), (020), and (−330) below 20 K, suggesting that the ferromagnetism probed in magnetization should be of short-range character. As discussed above, the short-range FM order can be attributed to the low occupancy of Cr (only ~31.7%) and Cr/Ga short-range ordering. Such short-range FM order is expected to produce very weak and diffusive magnetic scattering superimposed on the nuclear peaks, which is hard to be detected using unpolarized neutron diffraction at TOPAZ.

The direct band-gap semiconducting properties of $Cr_{0.32}Ga_{0.68}Te_{2.33}$ are revealed from the room-temperature Fourier-transform infrared (FTIR) spectroscopy measurements shown in Figure 5a,b. In FTIR measurements, the transmittance spectrum (T) was collected on the (0001) surface of $Cr_{0.32}Ga_{0.68}Te_{2.33}$. Interference fringes were observed at higher wavelengths, where the crystal is optically transparent (Figure 5a). The absorption coefficient α can be estimated using

$$I_{out} = I_{in}e^{-\alpha t} \quad (1)$$

where t is the thickness of the sample; I_{in} and I_{out} are the incident and transmitted intensities, respectively, and $T = \frac{I_{out}}{I_{in}}$. The Tauc plot of $(\alpha h\nu)^2$ vs photon energy E exhibits a linear behavior (Figure 5b), suggesting that $Cr_{0.32}Ga_{0.68}Te_{2.33}$ possesses a direct bandgap.[35] The optical bandgap is estimated to be 0.36 eV, as shown in Figure 5b. Its semiconducting properties are also verified in the measurements of the temperature dependence of resistivity (Supplementary Figure S3). Since the FM ordering temperature of this compound is relatively low (~20 K), the FM exchange interaction should be relatively weak, which should cause only a minor impact on the band gap.

Next, we will show that the semiconducting properties of $Cr_{0.32}Ga_{0.68}Te_{2.33}$ originate from the [Te(2), Te(3)] honeycomb layer, and its interplay with the 2D FM layer of Cr is likely to generate a spin-valley locked electronic state with valley polarization. In general, a honeycomb lattice could enable an active valley degree of freedom, e.g., graphene and monolayer TMDCs. Given that Te(2) and Te(3) form a quasi-2D honeycomb lattice in $Cr_{0.32}Ga_{0.68}Te_{2.33}$, the electronic

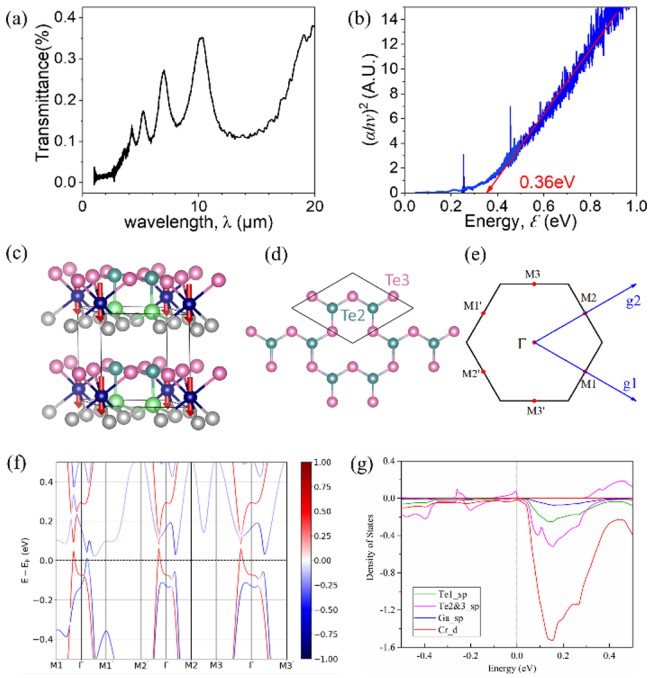

Figure 5. (a) Transmittance spectrum of $Cr_{0.32}Ga_{0.68}Te_{2.33}$ measured at room temperature. (b) Tauc plot of $Cr_{0.32}Ga_{0.68}Te_{2.33}$ showing the direct bandgap of 0.36 eV. (c) Schematic of crystal structure and out-of-plane ferromagnetism induced by the Cr sublattice for CrG_2Te_8 ($CrGa_2(Te1)_3(Te2)_2(Te3)_3$). Different sites of Te are shown with different colors. (d) Schematic of the Te2−Te3 plane. (e) High symmetry points in the Brillouin zone of the calculated band structure for CrG_2Te_8. (f) Band structure with magnetic Sz projection. (g) Density of states with projections on different ions and orbitals. Positive and negative values indicate the Sz directions. The Fermi level is indicated with a vertical dashed line.

structure of this compound may also have an active valley degree of freedom if its electronic states near the Fermi level are contributed by the S and P orbitals of Te(2) and Te(3). Further, considering the structure of $Cr_{0.32}Ga_{0.68}Te_{2.33}$ has broken inversion symmetry and heavy Te element brings in strong SOC, these traits, in combination with the valley degree of freedom, possibly generate a spin-valley locked state as seen in monolayer MoS_2. If this is the case, the 2D FM layer of Cr likely causes valley polarization. To theoretically demonstrate these possibilities, we performed DFT calculations to investigate the band structure for $Cr_{0.32}Ga_{0.68}Te_{2.33}$. Given that this new compound has a non-stoichiometric composition with a number of vacancies at [Te(2), Te(3)] and (Cr, Ga) sites, which makes DFT band structure calculations extremely difficult, we adopt an approximated structural model that assumes that (i) Te(3) sites are fully occupied while one-third of Te(2) sites form vacancies due to the formation of Cr octahedra and (ii) Cr atoms and Ga atoms are periodically distributed so that one supercell contains two Ga atoms and one Cr atom, as shown in Figure 5c. The composition corresponding to such an approximated structure is $CrGa_2Te_8$ ($CrGa_2(Te1)_3(Te2)_2(Te3)_3$), as shown in Figure 5c,d. Although it deviates from the refined composition $Cr_{0.32}Ga_{0.68}Te_{2.33}$ (which is equivalent to $CrGa_{2.13}Te_{7.28}$), it enables realistic calculations and captures the main characteristics of the band structure of this material. We employed the r^{2}SCAN density functional[36] together with an on-site Coulomb repulsion correction (U = 5 eV) on the d electrons of Cr. We

https://doi.org/10.1021/jacs.2c12848
J. Am. Chem. Soc. 2023, 145, 4683−4690

have also considered the out-of-plane ferromagnetism created by the 2D Cr layer in the calculations. Our calculated density of states (Figure 5f) demonstrates that the states near the Fermi level are indeed dominated by the Te-sp states contributed by the quasi-2D Te(2)-Te(3) honeycomb layer. The calculated band structure not only confirms that this material is characterized by valley-like electronic structures near the Fermi level but also reveals valley-dependent spin polarization, as shown in Figure 5f, where the spin polarization of energy bands is color coded. Those spin-polarized valleys are on the high symmetric paths of Γ-M1, Γ-M1′, Γ-M2, Γ-M2′, Γ-M3, and Γ-M3′ in the Brillion zone (Figure 5e). Furthermore, we also observed clear signs of valley polarization, as manifested by the asymmetry between spin-up and spin-down valleys (Figure 5f). Therefore, $Cr_{0.32}Ga_{0.68}Te_{2.33}$ is a possible candidate for bulk ferrovalley material, though our calculations do not fully capture the electronic properties of this material due to the simplified structure model used in the calculations (note that the calculated band structure suggests that this material is a half-semimetal rather than the experimentally observed semiconductor with a narrow direct band gap). In addition, the optical band gap of a layered material is typically smaller than its fundamental gap due to the large excitonic effect since the electron and hole are confined within layers.[37]

Prior studies on valleytronic states are mostly focused on 2D materials. There are only a few bulk materials that are found to have spin-valley locked states, including 3R-MoS_2,[38] 2H-$NbSe_2$,[39] and $BaMnSb_2$.[40] These materials do not show spontaneous valley polarization due to the lack of ferromagnetism. The possible valleytronic state with spontaneous valley polarization in $Cr_{0.32}Ga_{0.68}Te_{2.33}$ offers a rare opportunity to investigate the unique valley transport behavior in ferrovalley materials—the anomalous valley Hall effect (VHE).[22] As noted above, the VHE is unique to valleytronic states where valley-contrasted Berry curvature gives rise to opposite transverse velocities, resulting in spatial separation of carrier spin near the sample edges.[7] While the VHE has been extensively investigated in 2D valleytronic materials,[7,9,41−43] the anomalous VHE is a recently developed new concept, which is predicted to be present in only ferrovalley materials. Unlike the VHE, which arises from two types of carriers with opposite spins from two different valleys and does not produce charge Hall current, the anomalous VHE involves only one type of carrier from a single valley and induces additional charge Hall current and spin accumulation only near one sample edge. Theory predicts that anomalous VHE can be used to develop electrically reading and magnetically writing memory devices for valleytronic and spintronic applications. Although many 2D ferrovalley materials have been predicted as noted above, the anomalous VHE has not been demonstrated, possibly due to the difficulties of the synthesis of the predicted materials. Given that we have shown that $Cr_{0.32}Ga_{0.68}Te_{2.33}$ is a possible bulk ferrovalley material, it may be a promising candidate for the investigation of anomalous VHE using optical techniques such as Kerr rotation.

Finally, we would like to mention that the calculated interlayer binding energy of CrG_2Te_8 is ∼21 meV/Å^2, within the range of 13−21 meV/Å^2 previously found for typical layered vdW materials.[44] Such a small interlayer binding energy implies that this material can possibly be exfoliated to 2D atomically thin layers. To verify that, we performed mechanical exfoliations on $Cr_{0.32}Ga_{0.68}Te_{2.33}$ crystals and found they can be easily exfoliated down to a few layers and even to a monolayer (see Supplementary Figure S4). The access to 2D atomic crystals offers opportunities for electric-field control of the valleytronic state of $Cr_{0.32}Ga_{0.68}Te_{2.33}$.

3. SUMMARY

In summary, we have discovered a new vdW semiconducting compound $Cr_{0.32}Ga_{0.68}Te_{2.33,}$ with a narrow direct gap (∼0.36 eV) and out-of-plane ferromagnetism ($T_c \approx 20$ K). Through comprehensive studies using X-ray diffraction, neutron scattering, STEM, and SHG techniques, we find that this material crystallizes in a non-centrosymmetric trigonal structure with the space group of *P*3. This structure exhibits several interesting characteristics: (i) Cr and Ga form octahedral and tetrahedral coordination with Te, respectively, with the distributions of these Cr-octahedra and Ga-tetrahedra likely showing short-range order; (ii) this structure can be viewed as a naturally formed heterostructure: a quasi-2D [Te(2), Te(3)] layer with a honeycomb lattice stacked on the [(Cr, Ga)-Te(1)] slab, which shows short-range FM ordering. The DFT band structure calculations based on the simplified $CrGa_2Te_8$ structure model suggest that the 2D honeycomb lattice of [Te(2), Te(3)], in combination with the ferromagnetism generated by the Cr layer, inversion symmetry breaking, and the strong SOC from the heavy element Te, likely creates a unique spin-valley locked state with valley polarization near the Fermi level. Therefore, $Cr_{0.32}Ga_{0.68}Te_{2.33}$ offers a rare opportunity to explore the physics of the valleytronic state with spontaneous valley polarization, e.g., the anomalous valley Hall effect.

4. METHODS

4.1. Synthesis Method. The $Cr_{0.32}Ga_{0.68}Te_{2.33}$ single crystal was grown through the flux growth method. High-purity Cr powder, Ga ingot, and Te power were mixed with the mole ratio of Cr:Ga:Te = 1:8:36, and the mixture was loaded into an alumina crucible with a volume of 2 mL. The alumina crucible was put into a quartz tube and then covered by quartz fiber. The quartz tube with loaded source materials was then sealed under high vacuum. The sealed quartz tube was put into a muffle furnace and heated to 950 °C for 24 h to ensure homogeneous melting. The melt was then cooled to 660 °C in 150 h, followed by a slower cooling rate of 1 °C/h to 600 °C. The furnace was then quickly cooled down to 550 °C, and excessive Te and Ga flux was removed by centrifugation at 550 °C. Plate-like $Cr_{0.32}Ga_{0.68}Te_{2.33}$ single crystals with typical dimensions of 2 mm × 2 mm × 0.2 mm were obtained after centrifuging.

4.2. X-ray Diffraction Pattern and Magnetic Property Measurements. The phase purities of all samples selected for experiments were verified by single crystal XRD using Bruker Q8 Quest Eco at room temperature. The composition of the crystal is analyzed using X-ray energy-dispersive spectroscopy (EDS) measurements. The EDS mapping verified the homogeneity of the sample. Magnetic properties of the samples were measured using a superconducting quantum interference device (SQUID, quantum design).

4.3. Neutron Diffraction Experiments. Two neutron diffraction experiments were conducted at the single-crystal diffractometer TOPAZ, located at Oak Ridge National Laboratory, USA.[45] The same piece of plate-like crystal was used for these two experiments. A full data set was collected at 4, 30, 90, and 300 K. The crystal was rotated through a wide angle beyond 130° for survey on the elastic peaks in a wide range of reciprocal space. A CryoStream 700 Plus was used to collect the data at 90 and 300 K, whereas a cryogenic goniometer was adapted to cover the temperature region in 4 K < T < 300 K. The temperature dependence of a couple nuclear/magnetic peaks including low-Q (010), (−110), (−111), (020), (−330) and

https://doi.org/10.1021/jacs.2c12848
J. Am. Chem. Soc. 2023, 145, 4683−4690

high-Q (−432), (016), (−442) in 4 K < T < 30 K was measured by isothermal measurements at different temperatures going through T_C. The data were reduced using Mantid[46] and Python scripts available at TOPAZ.[47] The Bilbao Crystallographic Server[34] was employed to determine the symmetry-allowed magnetic structures. The crystallographic computing system JANA[48] was used to determine the crystal structure.

4.4. Transmission Electron Microscopy. The cross-sectional TEM sample along the [100] zone axis was prepared using the focused ion beam (FIB). The cross-sectional lamella was first extracted from the crystal surface by creating trenches with a 30 kV ion beam and performing the in situ lift-out with the micromanipulation needle. The lamella was then mounted onto the copper FIB/TEM grid and thinned down to 200 nm with a 30 kV ion beam and further down to electron transparency with a 5 kV ion beam. The final cleaning was performed with a 2 kV ion beam to remove the surface damage and reduce amorphization. The planar sample along [001] zone axis was prepared via a standard mechanical exfoliation technique from bulk $Cr_{0.32}Ga_{0.68}Te_{2.33}$ crystals, followed by transferring the exfoliated flakes to the TEM grid. High-angle annular dark field (HAADF) STEM was performed in a ThermoFisher Titan G2 equipped with a probe corrector. The acceleration voltage for the imaging was 80 kV to reduce the knock-on damage from the electron beam. The convergence angle and collection angle for the experiment are 21.5 and 60−200 mrad, respectively.

4.5. Transmittance Spectrum. The transmittance spectrum of $Cr_{0.32}Ga_{0.68}Te_{2.33}$ was measured from 1.24 eV (1 μm) to 0.062 eV (20 μm) with a Bruker Hyperion 3000 Microscope equipped with a 15× objective lens. The absorption coefficient was estimated from the transmittance spectrum. The bandgap, E_g, is related to the absorption coefficient α by $(\alpha h\nu)^{1/n} = A(h\nu - E_g)$, where A is a proportionality factor and n equals 0.5 and 2 for direct and indirect bandgaps, respectively.[49] By plotting $(\alpha h\nu)^n$ vs E with n = 0.5 or 2, one can identify the correct transition from the plot, giving the better fit. Then, the bandgap can be extracted by extrapolating the linear region to where $(\alpha h\nu)^n = 0$.

4.6. Second Harmonic Generation. SHG polarimetry was performed in reflection geometry with a 1550 nm fundamental laser generated by a Ti:sapphire femtosecond laser (100 fs, 1 kHz). The crystal was oriented such that $[2\bar{1}\bar{1}0]$ // lab X, $[01\bar{1}0]$ // lab Y and [0001] // lab Z, as shown in Figure 2a. The fundamental beam was linearly polarized and rotated by an angle of ψ using a half waveplate. The p-polarized (∥) and s-polarized (⊥) SHG responses were measured by a photomultiplier tube detector and fitted simultaneously to an analytical model based on point group 3.

4.7. First-Principles Computational Details. First-principles calculations based on density functional theory[50] are performed using the Vienna Ab Initio Simulation Package (VASP)[51] with the projector-augmented wave (PAW) method.[52,53] The r^{2}SCAN meta-GGA functional[36] is employed in this work due to its improved numerical stability and accuracy.[36,54] The valence configurations are taken as Cr: $3p^6 3d\ ^5 4s^1$, Ga: $3d^{10}4s^2 4p^1$, and Te: $5s^2 5p^4$. An energy cutoff of 500 eV is used to truncate the plane wave basis, together with a 1000 eV cut-off energy of the plane wave representation of the augmentation charges. Γ-centered meshes with a 6 × 6 × 6 mesh for the k-space sampling were used for the self-consistent calculation with an energy tolerance of 10^{-6} eV.

■ ASSOCIATED CONTENT

Supporting Information

The Supporting Information is available free of charge at https://pubs.acs.org/doi/10.1021/jacs.2c12848.

Additional experimental data including the HAADF-STEM image, SAED, temperature dependent resistivity, and image of the exfoliated thin flake (PDF)

Accession Codes

CCDC 2224113 contains the supplementary crystallographic data for this paper. These data can be obtained free of charge via www.ccdc.cam.ac.uk/data_request/cif, or by emailing data_request@ccdc.cam.ac.uk, or by contacting The Cambridge Crystallographic Data Centre, 12 Union Road, Cambridge CB2 1EZ, UK; fax: +44 1223 336033.

■ AUTHOR INFORMATION

Corresponding Authors

Nasim Alem − *Department of Materials Science and Engineering, Pennsylvania State University, University Park, Pennsylvania 16802, United States;* orcid.org/0000-0003-0009-349X; Email: nua10@psu.edu

Qiang Zhang − *Neutron Scattering Division, Oak Ridge National Laboratory, Oak Ridge, Tennessee 37831, United States;* orcid.org/0000-0003-0389-7039; Email: zhangq6@ornl.gov

Zhiqiang Mao − *Department of Physics and Department of Chemistry, Pennsylvania State University, University Park, Pennsylvania 16802, United States*; Email: zim1@psu.edu

Authors

Yingdong Guan − *Department of Physics, Pennsylvania State University, University Park, Pennsylvania 16802, United States;* orcid.org/0000-0002-1357-6258

Leixin Miao − *Department of Materials Science and Engineering, Pennsylvania State University, University Park, Pennsylvania 16802, United States*

Jingyang He − *Department of Materials Science and Engineering, Pennsylvania State University, University Park, Pennsylvania 16802, United States;* orcid.org/0000-0002-3886-3659

Jinliang Ning − *Department of Physics and Engineering Physics, Tulane University, New Orleans, Louisiana 70118, United States*

Yangyang Chen − *Department of Physics and 2-Dimensional Crystal Consortium, Pennsylvania State University, University Park, Pennsylvania 16802, United States*

Weiwei Xie − *Department of Chemistry, Michigan State University, East Lansing, Michigan 48824, United States*

Jianwei Sun − *Department of Physics and Engineering Physics, Tulane University, New Orleans, Louisiana 70118, United States;* orcid.org/0000-0002-2361-6823

Venkatraman Gopalan − *Department of Materials Science and Engineering, Pennsylvania State University, University Park, Pennsylvania 16802, United States*

Jun Zhu − *Department of Physics and 2-Dimensional Crystal Consortium, Pennsylvania State University, University Park, Pennsylvania 16802, United States;* orcid.org/0000-0001-8100-967X

Xiaoping Wang − *Neutron Scattering Division, Oak Ridge National Laboratory, Oak Ridge, Tennessee 37831, United States;* orcid.org/0000-0001-7143-8112

Complete contact information is available at: https://pubs.acs.org/10.1021/jacs.2c12848

Author Contributions

[+]Y.G. and L.M. contributed equally to this work.

Notes

The authors declare no competing financial interest.

■ ACKNOWLEDGMENTS

This work was supported by the US Department of Energy under grants DE-SC0019068 and DE-SC0014208 (support for

personnel, material discovery and synthesis, magnetic measurements, and data analyses). N.A. and L.M. acknowledge the support by NSF through the Pennsylvania State University Materials Research Science and Engineering Center (MRSEC) DMR-2011839 (2020− 2026). Y.C. and J.Z. acknowledge the support by the NSF-MIP 2DCC under award number DMR-2039351. J.H. and V.G. acknowledge the support by the NSF-MIP 2DCC under award number DMR-2210933. A portion of this research used resources at the Spallation Neutron Source, a DOE Office of Science User Facility operated by the Oak Ridge National Laboratory. The authors also acknowledge technical support of transport measurement by Wei Ning and technical assistance on the TOPAZ neutron experiments by Helen He.

■ ABBREVIATIONS

2D	two-dimensional
TMDC	transition metal dichalcogenide
SOC	spin-orbit coupling
FM	ferromagnetic
vdW	van der Waals
DFT	density functional theory
XRD	X-ray diffraction
EDS	energy-dispersive spectroscopy
HAADF	high-angle annular dark-field
STEM	scanning transmission electron microscopy
SAED	selected area electron diffraction
SHG	second harmonic generation
ZFC	zero-field cooling
FC	field cooling
FTIR	Fourier-transform infrared
VHE	valley Hall effect
SQUID	superconducting quantum interference device
FIB	focused ion beam
VASP	Vienna Ab Initio Simulation Package

■ REFERENCES

(1) Cao, T.; Wang, G.; Han, W.; Ye, H.; Zhu, C.; Shi, J.; Niu, Q.; Tan, P.; Wang, E.; Liu, B.; et al. Valley-selective circular dichroism of monolayer molybdenum disulphide. *Nat. Commun.* **2012**, *3*, 887.

(2) Jones, A. M.; Yu, H.; Ghimire, N. J.; Wu, S.; Aivazian, G.; Ross, J. S.; Zhao, B.; Yan, J.; Mandrus, D. G.; Xiao, D.; et al. Optical generation of excitonic valley coherence in monolayer WSe_2. *Nat. Nanotechnol.* **2013**, *8*, 634−638.

(3) Mak, K. F.; He, K.; Shan, J.; Heinz, T. F. Control of valley polarization in monolayer MoS_2 by optical helicity. *Nat. Nanotechnol.* **2012**, *7*, 494−498.

(4) Zeng, H.; Dai, J.; Yao, W.; Xiao, D.; Cui, X. Valley polarization in MoS_2 monolayers by optical pumping. *Nat. Nanotechnol.* **2012**, *7*, 490−493.

(5) Aivazian, G.; Gong, Z.; Jones, A. M.; Chu, R.-L.; Yan, J.; Mandrus, D. G.; Zhang, C.; Cobden, D.; Yao, W.; Xu, X. Magnetic control of valley pseudospin in monolayer WSe_2. *Nat. Phys.* **2015**, *11*, 148−152.

(6) Xu, X.; Yao, W.; Xiao, D.; Heinz, T. F. Spin and pseudospins in layered transition metal dichalcogenides. *Nat. Phys.* **2014**, *10*, 343−350.

(7) Xiao, D.; Liu, G.-B.; Feng, W.; Xu, X.; Yao, W. Coupled Spin and Valley Physics in Monolayers of MoS_2 and Other Group-VI Dichalcogenides. *Phys. Rev. Lett.* **2012**, *108*, No. 196802.

(8) Onga, M.; Zhang, Y.; Ideue, T.; Iwasa, Y. Exciton Hall effect in monolayer MoS_2. *Nat. Mater.* **2017**, *16*, 1193−1197.

(9) Mak, K. F.; McGill, K. L.; Park, J.; McEuen, P. L. The valley Hall effect in MoS_2 transistors. *Science* **2014**, *344*, 1489−1492.

(10) Schaibley, J. R.; Yu, H.; Clark, G.; Rivera, P.; Ross, J. S.; Seyler, K. L.; Yao, W.; Xu, X. Valleytronics in 2D materials. *Nat. Rev. Mater.* **2016**, *1*, 16055.

(11) Ye, Z.; Sun, D.; Heinz, T. F. Optical manipulation of valley pseudospin. *Nat. Phys.* **2017**, *13*, 26−29.

(12) Cai, T.; Yang, S. A.; Li, X.; Zhang, F.; Shi, J.; Yao, W.; Niu, Q. Magnetic control of the valley degree of freedom of massive Dirac fermions with application to transition metal dichalcogenides. *Phys. Rev. B* **2013**, *88*, No. 115140.

(13) Singh, N.; Schwingenschlögl, U. A Route to Permanent Valley Polarization in Monolayer MoS_2. *Adv. Mater.* **2017**, *29*, 1600970.

(14) Peng, R.; Ma, Y.; Zhang, S.; Huang, B.; Dai, Y. Valley Polarization in Janus Single-Layer MoSSe via Magnetic Doping. *J. Phys. Chem. Lett.* **2018**, *9*, 3612−3617.

(15) Cheng, Y. C.; Zhang, Q. Y.; Schwingenschlögl, U. Valley polarization in magnetically doped single-layer transition-metal dichalcogenides. *Phys. Rev. B* **2014**, *89*, No. 155429.

(16) Zhao, C.; Norden, T.; Zhang, P.; Zhao, P.; Cheng, Y.; Sun, F.; Parry, J. P.; Taheri, P.; Wang, J.; Yang, Y.; et al. Enhanced valley splitting in monolayer WSe_2 due to magnetic exchange field. *Nat. Nanotechnol.* **2017**, *12*, 757−762.

(17) Norden, T.; Zhao, C.; Zhang, P.; Sabirianov, R.; Petrou, A.; Zeng, H. Giant valley splitting in monolayer WS_2 by magnetic proximity effect. *Nat. Commun.* **2019**, *10*, 4163.

(18) Zhang, Q.; Yang, S. A.; Mi, W.; Cheng, Y.; Schwingenschlögl, U. Large Spin-Valley Polarization in Monolayer $MoTe_2$ on Top of EuO(111). *Adv. Mater.* **2016**, *28*, 959−966.

(19) Xu, L.; Yang, M.; Shen, L.; Zhou, J.; Zhu, T.; Feng, Y. P. Large valley splitting in monolayer WS_2 by proximity coupling to an insulating antiferromagnetic substrate. *Phys. Rev. B* **2018**, *97*, No. 041405.

(20) Hu, T.; Zhao, G.; Gao, H.; Wu, Y.; Hong, J.; Stroppa, A.; Ren, W. Manipulation of valley pseudospin in WSe_2/ CrI_3 heterostructures by the magnetic proximity effect. *Phys. Rev. B* **2020**, *101*, No. 125401.

(21) Zhong, D.; Seyler, K. L.; Linpeng, X.; Cheng, R.; Sivadas, N.; Huang, B.; Schmidgall, E.; Taniguchi, T.; Watanabe, K.; McGuire, M. A.; et al. Van der Waals engineering of ferromagnetic semiconductor heterostructures for spin and valleytronics. *Sci. Adv.* **2017**, *3*, No. e1603113.

(22) Tong, W.-Y.; Gong, S.-J.; Wan, X.; Duan, C.-G. Concepts of ferrovalley material and anomalous valley Hall effect. *Nat. Commun.* **2016**, *7*, 13612.

(23) Zhao, P.; Ma, Y.; Lei, C.; Wang, H.; Huang, B.; Dai, Y. Single-layer $LaBr_2$: Two-dimensional valleytronic semiconductor with spontaneous spin and valley polarizations. *Appl. Phys. Lett.* **2019**, *115*, 261605.

(24) Sheng, K.; Yuan, H.-K.; Wang, Z.-Y. Monolayer gadolinium halides, GdX_2 (X = F, Cl, Br): intrinsic ferrovalley materials with spontaneous spin and valley polarizations. *PCCP* **2022**, *24*, 3865−3874.

(25) Cheng, H.-X.; Zhou, J.; Ji, W.; Zhang, Y.-N.; Feng, Y.-P. Two-dimensional intrinsic ferrovalley GdI_2 with large valley polarization. *Phys. Rev. B* **2021**, *103*, No. 125121.

(26) Song, Z.; Sun, X.; Zheng, J.; Pan, F.; Hou, Y.; Yung, M.-H.; Yang, J.; Lu, J. Spontaneous valley splitting and valley pseudospin field effect transistors of monolayer $VAgP_2Se_6$. *Nanoscale* **2018**, *10*, 13986−13993.

(27) Peng, R.; Ma, Y.; Xu, X.; He, Z.; Huang, B.; Dai, Y. Intrinsic anomalous valley Hall effect in single-layer Nb_3I_8. *Phys. Rev. B* **2020**, *102*, No. 035412.

(28) Du, W.; Ma, Y.; Peng, R.; Wang, H.; Huang, B.; Dai, Y. Prediction of single-layer $TiVI_6$ as a promising two-dimensional valleytronic semiconductor with spontaneous valley polarization. *J. Mater. Chem. C* **2020**, *8*, 13220−13225.

(29) Cui, Q.; Zhu, Y.; Liang, J.; Cui, P.; Yang, H. Spin-valley coupling in a two-dimensional VSi_2N_4 monolayer. *Phys. Rev. B* **2021**, *103*, No. 085421.

https://doi.org/10.1021/jacs.2c12848
J. Am. Chem. Soc. 2023, 145, 4683−4690

(30) Li, S.; He, J.; Grajciar, L.; Nachtigall, P. Intrinsic valley polarization in 2D magnetic MXenes: surface engineering induced spin-valley coupling. *J. Mater. Chem. C* **2021**, *9*, 11132−11141.
(31) Zang, Y.; Ma, Y.; Peng, R.; Wang, H.; Huang, B.; Dai, Y. Large valley-polarized state in single-layer NbX_2 (X = S, Se): Theoretical prediction. *Nano Res.* **2021**, *14*, 834−839.
(32) Zhang, C.; Nie, Y.; Sanvito, S.; Du, A. First-Principles Prediction of a Room-Temperature Ferromagnetic Janus VSSe Monolayer with Piezoelectricity, Ferroelasticity, and Large Valley Polarization. *Nano Lett.* **2019**, *19*, 1366−1370.
(33) Jiang, P.; Kang, L.; Li, Y.-L.; Zheng, X.; Zeng, Z.; Sanvito, S. Prediction of the two-dimensional Janus ferrovalley material LaBrI. *Phys. Rev. B* **2021**, *104*, No. 035430.
(34) Aroyo, M. I.; Perez-Mato, J. M.; Capillas, C.; Kroumova, E.; Ivantchev, S.; Madariaga, G.; Kirov, A.; Wondratschek, H. Bilbao Crystallographic Server: I. Databases and crystallographic computing programs. *Z. fur Krist. - Cryst. Mater.* **2006**, *221*, 15−27.
(35) Makuła, P.; Pacia, M.; Macyk, W. How To Correctly Determine the Band Gap Energy of Modified Semiconductor Photocatalysts Based on UV−Vis Spectra. *J. Phys. Chem. Lett.* **2018**, *9*, 6814−6817.
(36) Furness, J. W.; Kaplan, A. D.; Ning, J.; Perdew, J. P.; Sun, J. Accurate and Numerically Efficient r^2SCAN Meta-Generalized Gradient Approximation. *J. Phys. Chem. Lett.* **2020**, *11*, 8208−8215.
(37) Choi, J.-H.; Cui, P.; Lan, H.; Zhang, Z. Linear Scaling of the Exciton Binding Energy versus the Band Gap of Two-Dimensional Materials. *Phys. Rev. Lett.* **2015**, *115*, No. 066403.
(38) Suzuki, R.; Sakano, M.; Zhang, Y. J.; Akashi, R.; Morikawa, D.; Harasawa, A.; Yaji, K.; Kuroda, K.; Miyamoto, K.; Okuda, T.; et al. Valley-dependent spin polarization in bulk MoS_2 with broken inversion symmetry. *Nat. Nanotechnol.* **2014**, *9*, 611−617.
(39) Bawden, L.; Cooil, S. P.; Mazzola, F.; Riley, J. M.; Collins-McIntyre, L. J.; Sunko, V.; Hunvik, K. W. B.; Leandersson, M.; Polley, C. M.; Balasubramanian, T.; et al. Spin−valley locking in the normal state of a transition-metal dichalcogenide superconductor. *Nat. Commun.* **2016**, *7*, 11711.
(40) Liu, J. Y.; Yu, J.; Ning, J. L.; Yi, H. M.; Miao, L.; Min, L. J.; Zhao, Y. F.; Ning, W.; Lopez, K. A.; Zhu, Y. L.; et al. Spin-valley locking and bulk quantum Hall effect in a noncentrosymmetric Dirac semimetal BaMnSb2. *Nat. Commun.* **2021**, *12*, 4062.
(41) Feng, W.; Yao, Y.; Zhu, W.; Zhou, J.; Yao, W.; Xiao, D. Intrinsic spin Hall effect in monolayers of group-VI dichalcogenides: A first-principles study. *Phys. Rev. B* **2012**, *86*, No. 165108.
(42) Ezawa, M. Valley-Polarized Metals and Quantum Anomalous Hall Effect in Silicene. *Phys. Rev. Lett.* **2012**, *109*, No. 055502.
(43) Pan, H.; Li, Z.; Liu, C.-C.; Zhu, G.; Qiao, Z.; Yao, Y. Valley-Polarized Quantum Anomalous Hall Effect in Silicene. *Phys. Rev. Lett.* **2014**, *112*, No. 106802.
(44) Björkman, T.; Gulans, A.; Krasheninnikov, A. V.; van der Nieminen, R. M. Waals Bonding in Layered Compounds from Advanced Density-Functional First-Principles Calculations. *Phys. Rev. Lett.* **2012**, *108*, No. 235502.
(45) Coates, L.; Cao, H. B.; Chakoumakos, B. C.; Frontzek, M. D.; Hoffmann, C.; Kovalevsky, A. Y.; Liu, Y.; Meilleur, F.; Santos, A. M. d.; Myles, D. A. A.; et al. A suite-level review of the neutron single-crystal diffraction instruments at Oak Ridge National Laboratory. *Rev. Sci. Instrum.* **2018**, *89*, No. 092802.
(46) Arnold, O.; Bilheux, J. C.; Borreguero, J. M.; Buts, A.; Campbell, S. I.; Chapon, L.; Doucet, M.; Draper, N.; Ferraz Leal, R.; Gigg, M. A.; et al. Mantid—Data analysis and visualization package for neutron scattering and μ SR experiments. *Nuclear Instruments and Methods in Physics Research Section A: Accelerators, Spectrometers, Detectors and Associated Equipment* **2014**, *764*, 156−166.
(47) Schultz, A. J.; Jorgensen, M. R. V.; Wang, X.; Mikkelson, R. L.; Mikkelson, D. J.; Lynch, V. E.; Peterson, P. F.; Green, M. L.; Hoffmann, C. M. Integration of neutron time-of-flight single-crystal Bragg peaks in reciprocal space. *J. Appl. Crystallogr.* **2014**, *47*, 915−921.
(48) Petříček, V.; Dušek, M.; Palatinus, L. Crystallographic Computing System JANA2006: General features. *Z. fur Krist. - Cryst. Mater.* **2014**, *229*, 345−352.
(49) Tauc, J. Optical properties and electronic structure of amorphous Ge and Si. *Mater. Res. Bull.* **1968**, *3*, 37−46.
(50) Kohn, W.; Sham, L. J. Self-consistent equations including exchange and correlation effects. *Phys. Rev.* **1965**, *140*, A1133.
(51) Kresse, G.; Furthmüller, J. Efficient iterative schemes for ab initio total-energy calculations using a plane-wave basis set. *Phys. Rev. B* **1996**, *54*, 11169.
(52) Blöchl, P. E. Projector augmented-wave method. *Phys. Rev. B* **1994**, *50*, 17953.
(53) Kresse, G.; Joubert, D. From ultrasoft pseudopotentials to the projector augmented-wave method. *Phys. Rev. B* **1999**, *59*, 1758.
(54) Ning, J.; Furness, J. W.; Sun, J. Reliable Lattice Dynamics from an Efficient Density Functional Approximation. *Chem. Mater.* **2022**, *34*, 2562−2568.

https://doi.org/10.1021/jacs.2c12848
J. Am. Chem. Soc. 2023, 145, 4683−4690